RSC Advances

PAPER

View Article Online
View Journal | View Issue

Cite this: *RSC Adv.*, 2025, **15**, 8580

Catalytic reduction of aldehydic and nitro groups of nitro-benzaldehyde derivatives by silver nanoparticle–containing smart alginate-poly(*N*-isopropylacrylamide-methacrylic acid) microgels†

Muhammad Arif, *[a] Fatima Tahir,[a] Tajamul Hussain,[bc] Salman Alrokayan[c] and Toheed Akhter *[d]

Aromatic compounds containing aldehyde and nitro groups are very toxic to human health. Moreover, complete degradation of these compounds is not possible. Therefore, these compounds are converted into less toxic but more useful hydroxy-methyl aniline (HMA) derivatives. This conversion is performed using a suitable catalyst and a reducing agent. Therefore, alginate-poly(*N*-isopropylacrylamide-methacrylic acid) (AN-P(NIPAM-MAAc)) (AN-P(NM)) microgels were synthesized *via* a free radical precipitation polymerization (FRPP) method and were used as a micro-reactor for synthesis of silver (Ag) nanoparticles (NPs) into the polymeric network using *in situ* reduction methods. The synthesized AN-P(NM) microgels and Ag-AN-P(NM) hybrid microgels were characterized through SEM, FTIR, TEM, XRD, UV-vis spectroscopy, and EDX. Ag-AN-P(NM) exhibited temperature- and pH-responsive behavior as well as long-term stability of Ag nanoparticles in a polymeric network of AP(NM). Catalytic reduction of 4-nitrobenzaldehyde (4NBA) was evaluated under different conditions, such as different contents of Ag-AN-P(NM), 4NBA concentrations, temperatures, and concentrations of $NaBH_4$. The Ag-AP(NM) hybrid microgels catalytically reduced 3-nitrobenzaldehyde (3NBA), 4NBA, and 3,5-dinitrobanzaldehyde (3,5DNBA) into their corresponding HA compounds in a water medium. The apparent rate constant (k_{ob}) values for 3NBA, 4NBA, and 3,5DNBA were found to be 1.73 min^{-1}, 1.48 min^{-1}, and 1.19 min^{-1}, respectively. Ag-AP(NM) exhibited outstanding catalytic efficiency, recyclability, and stability as well as retained its performance across multiple cycles.

Received 30th January 2025
Accepted 7th March 2025

DOI: 10.1039/d5ra00713e

rsc.li/rsc-advances

1. Introduction

Water pollution poses a significant threat to aquatic ecosystems and human health.[1–4] Key contributors to water pollution include various chemical substances such as nitroarenes,[5,6] heavy metal ions,[7,8] dyes,[9,10] pesticides,[11,12] and aromatic aldehydes.[13,14] Among these, benzaldehyde derivatives and nitroarenes are the primary sources of contamination. The complete removal of these compounds from water is an important task for researchers. This issue can be solved by converting more toxic nitro-benzaldehyde (NBA) derivatives into their corresponding less toxic amino-benzyl alcohol (ABlA) derivatives in an aqueous medium.[15–17] Arylamines and phenol derivatives are essential precursors for the production of dyes,[18–20] pharmaceuticals,[21,22] polymers,[23,24] biochemicals,[25,26] antioxidants,[27,28] and other fine chemicals.[29–32] An efficient approach for this conversion is catalytic reduction using a reductant[33–37] along with an appropriate catalyst and reducing agent, such as $NaBH_4$. Both types of heterogeneous[38–40] and homogeneous[41,42] catalysts can be employed for these reactions. However, homogeneous catalytic systems have limitations, such as toxicity, limited availability, high costs, and recycling difficulties. Alternatively, heterogeneous catalysts face the challenge of catalyst poisoning. Nanocatalysts have emerged as a better solution for addressing the deficiencies of both catalytic systems. Therefore, metal NPs have attracted attention for the conversion of nitro-benzaldehyde (NBA) derivatives into its corresponding amino-benzyl alcohol (ABlA) using reductants.[43–45] The most efficient NPs are composed of expensive metals, such as Pd,[46] Au,[47] Rh,[48] and Pt.[49] These metal NPs are commonly employed as catalysts for these transformations

[a]*Department of Chemistry, School of Science, University of Management and Technology, Lahore 54770, Pakistan. E-mail: Muhammadarif2861@yahoo.com; Muhammadarif@umt.edu.pk*

[b]*Center of Excellence in Biotechnology Research, King Saud University, Riyadh 11451, Saudi Arabia*

[c]*Research Chair for Biomedical Application of Nanomaterials, Biochemistry Department, College of Science, King Saud University, Riyadh 11451, Saudi Arabia*

[d]*Department of Chemical and Biological Engineering, Gachon University, Seongnam-13120, Republic of Korea. E-mail: toheed@gachon.ac.kr*

† Electronic supplementary information (ESI) available. See DOI: https://doi.org/10.1039/d5ra00713e

in water. Nonetheless, the industrial use of these metal nanoparticles is hampered by the high cost of their precursor salts. In addition, the reduction of NBA derivatives using nanoparticles relies on the presence of highly volatile H_2 (produced by the reductant), which poses safety concerns. An alternative method for this conversion reaction is transfer hydrogenation. This method diminishes the need for H_2 for the conversion reaction. However, this approach often requires organic solvents or solvent mixtures at elevated temperatures, complicating catalyst recycling after the reaction. Consequently, the conversion of NBA derivatives into their corresponding ABA using metal NPs has emerged as the preferred method.[50–52] Both noble (costly)[49,53] and non-noble (cheap)[54–57] metal NPs can be employed for these reaction conversions. Although NPs of cheap metals are also explored as catalysts for the reduction of NBA derivatives, they often face issues with instability, low surface area, and poor recyclability. This challenge can be tackled by utilizing cost-effective silver (Ag) nanoparticles, which are less expensive than other noble metals. These Ag nanoparticles demonstrate high efficiency in the catalytic reduction of ABA derivatives with $NaBH_4$. Ag nanoparticles can be used to make composite materials.[58–64] The catalytic activity of these composites is also very interesting, but the long-term use of these Ag nanoparticles is still an issue. This challenge can be resolved using various supporting matrices, such as microgels (crosslinked organic polymers),[65–67] block copolymers,[68] ionic liquids,[69] dendrimers,[70] and surfactants.[71] These matrices are used to stabilize Ag nanoparticles and enhance their catalytic performance. Microgels are the best of these stabilizing matrices.

Microgels serve as capping agents within the supporting matrix, providing stabilization and enhancing the performance of silver (Ag) nanoparticles.[72–74] Consequently, composites of Ag nanoparticles embedded in microgels have attracted considerable attention. These nanoparticles are stabilized within the network of microgels through donor–acceptor attraction with different microgel functional groups.[75] Nonetheless, the lack of biodegradability in conventional microgels poses a significant challenge, which is tackled using biodegradable and nontoxic alginate (AN).[76] Methacrylic acid (MAAc)[77] and *N*-isopropylacrylamide (NIPAM)[78] are used to impart pH- and temperature-responsive properties to the microgel composites, respectively. MAAc also facilitates the loading of Ag^+ ions to its maximum level, which is then converted into Ag NPs after reduction within the microgels.[79,80] To the best of the available literature, no studies have reported the fabrication of Ag nanoparticles in pH- and temperature-dependent AN-P(NM) systems for the conversion of NBA derivatives into their corresponding ABA.

This study focuses on the fabrication, characterization, and catalytic performance of Ag NPs encapsulated within AN-P(NM) microgels. Several ABA derivatives were obtained through the catalytic reduction of corresponding NBA derivatives in an aqueous medium under mild conditions. Ag-AN-P(NM) was applied as a catalyst in diverse reaction environments to evaluate the kinetic factors. Additionally, a reduction mechanism of NBA derivatives was developed to explain the alteration of NBA derivatives into ABA with Ag-AN-P(NM) and $NaBH_4$.

2. Materials and methods

2.1. Materials

Ammonium per sulfate (APS) (99%), *N*,*N*-methylene bis acrylamide (MBA) (99%), (*N*-isopropylmethacrylamide (NIPM)) (98%), sodium alginate (SAN), sodium dodecyl sulfate (SDS) (98%), sodium borohydride ($NaBH_4$) (98%), 3NBA (99%), 4NBA (98%), 3,5DNBA (97%) and silver nitrate ($AgNO_3$) (99%) were obtained from Sigma Aldrich, Germany. During AN-P(NM) and Ag-AN-P(NM) synthesis, and during catalysis, deionized water (DIW) was used. A dialysis membrane was used for AN-P(NM) and Ag-AN-P(NM) purification and was obtained from Scharlu.

2.2. AN-P(NM) and Ag-AN-P(NM) synthesis

AN-P(NM) microgels were synthesized using the FRPP method, as shown in Fig. 1. A mixture of 0.503 g of NIPAM, 0.503 g of sodium alginate, 0.00423 g of MAAc, 0.041 g of MBA, and 0.085 g of SDS was prepared in 93 mL of DIW within a three-neck flask and stirred with an increasing temperature of 343 K under a nitrogen atmosphere. After 30 min of maintaining the temperature, 7 mL of APS (0.08 mM) solution was poured dropwise into the mixture with continuous stirring. The reaction continued for 4 h under the same conditions. The appearance of a milky color signified the formation of AN-P(CM). The product was then dialyzed for four days to obtain a pure sample.

Ag-AN-P(NM) was synthesized using an *in situ* reduction approach. A 50 mL dispersion of AN-P(NM) was diluted by adding 50 mL DIW into a three-neck flask and stirred at room temperature for 30 min. Subsequently, $AgNO_3$ (5 mL, 1 mM) was added and stirred for 1 h under a nitrogen atmosphere. To reduce Ag^+ ions, $NaBH_4$ (5 mL, 5 mM) was introduced under the same conditions. The color changes from milky white to yellow. This in turn showed the formation of silver NPs. The mixture was dialyzed for 1.5 h to ensure purification.

2.3. Characterization techniques

AN-P(NM) microgels and Ag-AN-P(NM) hybrid microgels were characterized by applying the FTIR technique (RXI FTIR spectrometer) to estimate their structural hierarchies. The UV-vis spectra of the dispersion of these products were obtained using a UV-visible/NIR spectrophotometer (V-770, JASCO). One drop of the sample was placed on a coated copper grid and dried in air to record the TEM images. Then, images were obtained using an FEI TECNAI microscope operating at 120 kV. The elemental composition of AN-P(NM) and Ag-AN-P(NM) was analyzed using a Nova-Nano-SEM microscope. XRD analysis of the samples was carried out using a Bruker D2-Phaser instrument. The characterization conditions included a scan step size (sss) of 0.025 and a time per step (tps) of 0.4.

2.4. Reduction of NBA derivatives

3NBA, 4NBA, and 3,5-DNBA were reduced catalytically using $NaBH_4$ with Ag-AN-P(NM) at an ambient temperature (301 K). The catalytic reduction of 4NBA was performed under diverse

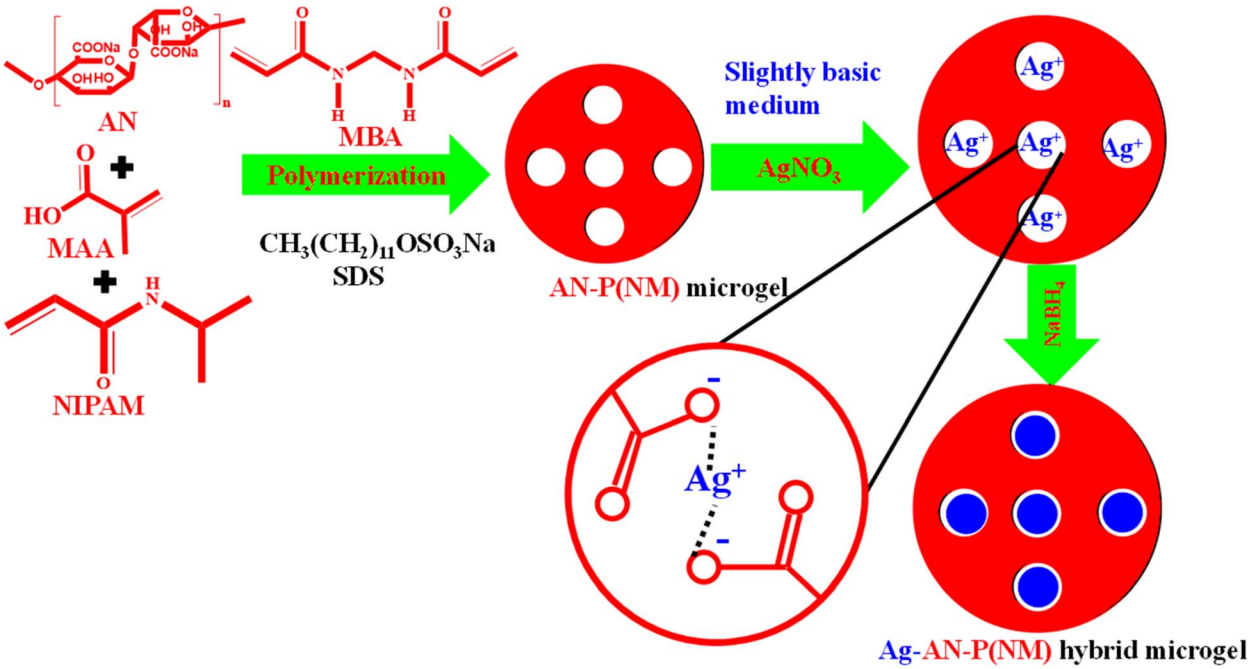

Fig. 1 Synthesis of alginate-poly(*N*-isopropylacrylamide-methacrylic acid) Ag-AN-P(NM) hybrid microgels containing alginate-poly(*N*-isopropylacrylamide-methacrylic acid) AN-P(CN) and Ag nanoparticles.

reaction conditions, such as $NaBH_4$ (1.97–6.71 mM), temperature (297–313 K), Ag-AN-P(NM) dose (0.59–1.78 mg mL^{-1}), and substrate (0.03–0.15 mM). The reduction of 3NBA and 3,5-DNBA was also performed under similar conditions.

3. Results and discussion

3.1. AN-P(NM) microgel and Ag-AN-P(NM) hybrid microgel synthesis

AN-P(NM) was prepared by applying the FRPP method, as shown in Fig. 1.[81] A high temperature (343 K) was used to generate micro gelation and prevent the formation of macro gelation.[82] SDS was utilized to control the size and size distribution of the micro particles. The APS solution was added dropwise to start polymerization and control the crosslinking density throughout the network. The Ag^+ ions came into the sieves of a crosslinked network of AN-P(NM) microgels from a water medium owing to electrostatic interaction present between the microgel networks (negatively charged) and Ag^+ ions (positively charged). These loaded ions were *in situ* reduced into Ag^0 atoms with $NaBH_4$. These atoms start to coagulate in the sieves to form a cluster in the nano-range.

3.2. Characterizations

The functional hierarchy in the network of AN-P(NM) microgels and Ag-AN-P(NM) hybrid microgels was identified using the FTIR technique, as shown in Fig. 2(A). A broad peak appeared at 3308 cm^{-1} in AN-P(NM) and Ag-AN-P(NM) hybrid microgels, indicating the presence of –OH and $–NH_2$ groups in their networks. These groups have a high affinity for water molecules. Some amounts of water molecules were also present in the network. Therefore, a broad peak with high intensity was obtained. The peak intensity was greater in AN-P(NM) compared to Ag-AN-P(NM), resulting in AN-P(CM) having a greater affinity towards water molecules than Ag-AN-P(NM). This is because some space is occupied with Ag nanoparticles in Ag-AN-P(NM), while more empty space is available in AN-P(NM). The C=O group peaks appeared at 1625 cm^{-1} in Ag-AN-P(NM) and AN-P(NM). These peaks were present at the same position, which indicated that all loaded Ag^+ ions shifted completely into Ag^0 after the *in situ* reduction approach. The intensity of all peaks of Ag-AN-P(NM) was slightly less than that of the peaks of AN-P(NM) owing to less availability of space for water molecules after insertion and formation of Ag NPs in the network of AN-P(NM).[83]

The composition of elements in the network of AN-P(NM) and Ag-AN-P(NM) was analyzed using the EDX, as shown in Fig. 2(B) and (C), respectively. The percentage composition of each element is shown in Fig. 2(B and C). Both spectra of AN-P(NM) and Ag-AN-P(NM) indicate that oxygen (O) and carbon (C) were present in the network of AN-P(NM) and Ag-AN-P(NM). However, Ag NPs were detected exclusively in the Ag-AN-P(NM) spectrum, as shown in Fig. 2(C). These results confirm that Ag NPs exist only in Ag-AN-P(NM) and not in AN-P(NM).

The degree of crystallinity in AN-P(NM) and Ag-AN-P(NM) was identified using the XRD technique, as depicted in Fig. 2(D). The XRD spectrum of AN-P(NM) showed a broad peak, indicating that the AN-P(NM) was not crystalline in nature. Sharp peaks were obtained in the spectrum of Ag-AN-P(NM), which showed that crystallinity was present in Ag-AN-P(NM) owing to the existence of Ag NPs in the structure of AN-P(NM) microgels. In this way, the XRD spectra of AN-P(NM) and Ag-

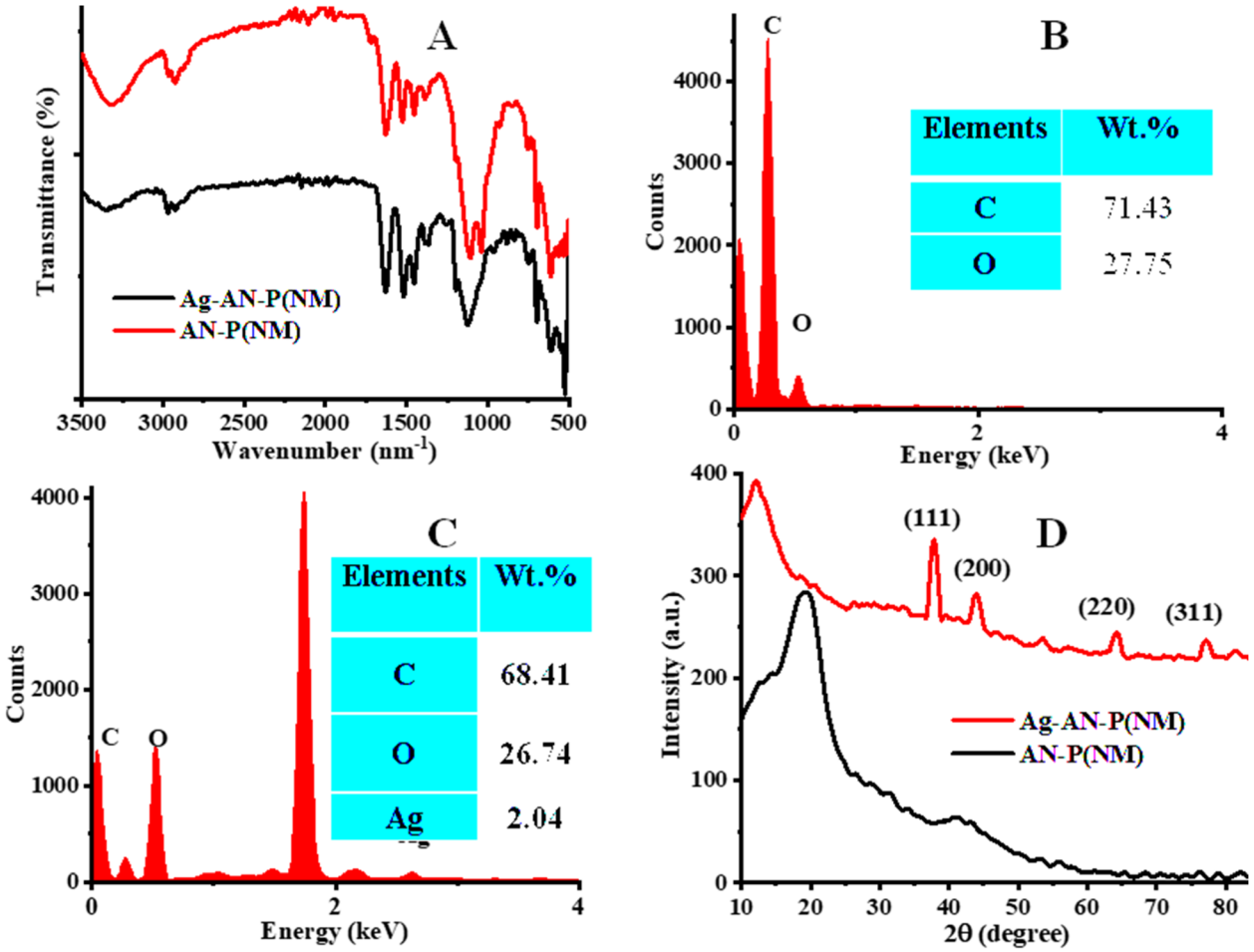

Fig. 2 (A) FTIR spectra of AN-P(CN) and Ag-AN-P(CN), (B and C) EDX results of AN-P(NM) and Ag-AN-P(NM), respectively, and (D) XRD spectra of AN-P(NM) and Ag-AN-P(NM).

AN-P(NM) indicated the presence of Ag NPs in AN-P(NM). The Ag NPs of Ag-AN-P(NM) exhibit a face-centered cubic structure, as indicated through high-intensity peaks. These peaks were detected at 2θ angles of 37.88°, 44.25°, 64.54°, and 77.68°, corresponding to the [111], [200], [220], and [311] crystal planes, respectively. Similar peaks with similar positions of Ag nanoparticles were observed by Begum *et al.*[36] and Siddiq *et al.*,[80] and they reported that the Ag nanoparticles have a face-centered cubic shape.

The existence of Ag NPs in the sieves of the network of AN-P(NM) microgels was studied using a UV-vis spectrophotometer. For this performance, the dispersion of both AN-P(NM) and Ag-AN-P(NM) was run in a UV-vis spectrophotometer, and the obtained spectra of both are shown in Fig. 3(A). No clear peak was obtained in the spectrum of AN-P(NM), while a clear peak was present in the Ag-AN-P(NM) spectrum at 402 nm owing to the surface plasmon resonance (λ_{SPR}) of Ag NPs, which were present only in Ag-AN-P(NM) but not in AN-P(NM). The single peak of λ_{SPR} indicated that the Ag nanoparticles are spherical.[84]

The Ag NP stability in the network of AN-P(NM) microgels was checked by storing the dispersion of Ag-AN-P(NM) hybrid microgels in the dark and running their spectra after an interval. The obtained UV-vis spectra of Ag-AN-P(NM) hybrid microgels are illustrated in Fig. 3(B). No change was noted in the peak of λ_{SPR} in the spectra of Ag-AN-P(NM) even after 7 weeks, which indicated that the Ag NPs were stabilized in the polymeric network for a long time.

The surface morphologies of AN-P(NM) and Ag-AN-P(NM) were identified using the SEM technique. The surface of AN-P(NM) is porous and rough, as shown in Fig. 4(A and B). The confirmation of the existence of Ag NPs in AN-P(NM) was done with the help of TEM images. The morphology and size of the Ag NPs were also determined through TEM analysis, as shown in Fig. 4(C) and (D). The shape of the Ag NPs was not perfectly spherical. A similar spherical shape was indicated by the UV-vis spectrum of Ag-AN-P(NM) and was obtained from the TEM images. 16.23 ± 5.12 nm was the diameter of Ag NPs, which were present in the network of AN-P(NM) microgels.

The stimuli-responsive behavior of microgels on the λ_{SPR} (localized surface plasmon resonance) of Ag NPs was investigated. The effect of temperature on the λ_{SPR} shift of Ag NPs owing to the deswelling and swelling properties of the microgels is presented in Fig. 1S(B),† while the effect of pH is shown in Fig. 1S(B).† Fig. 1S(A)† demonstrates that Ag nanoparticles encapsulated within AN-P(NM) are stable across various temperatures.

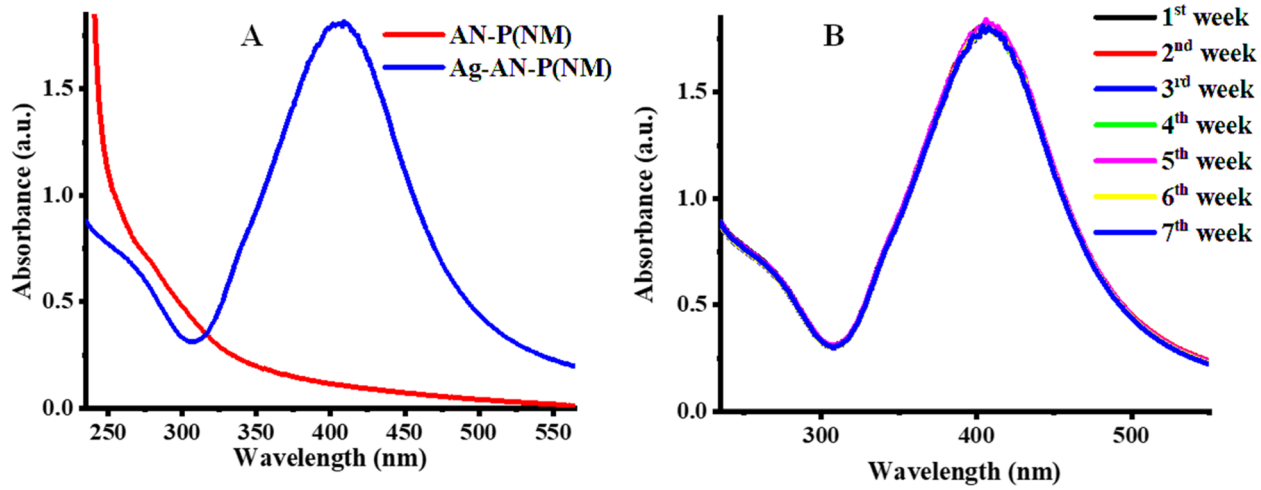

Fig. 3 UV-vis spectra of (A) AN-P(NM) and Ag-AN-P(NM), and (B) Ag-AN-P(NM) after different time intervals.

The effect of temperature on the value of λ_{SPR}s of Ag NPs encapsulated in AN-P(NM) was studied, as depicted in Fig. 1S(A)† at a slightly acidic pH (pH 6.5). The data obtained show that the Ag NPs remained stable across a wide range of temperatures (294–314 K). The λ_{SPR} value shifted from 398 nm to 418 nm as the temperature increased, which can be attributed to shifts in the value of the refractive index and interparticle distance. No significant red shift was observed when the temperature increased from 294 to 306 K, but a pronounced red shift occurred as the temperature increased from 306 K to 314 K. It was noted that the volume phase transition temperature (VPTT) value of AN-P(NM) was about 305 K.

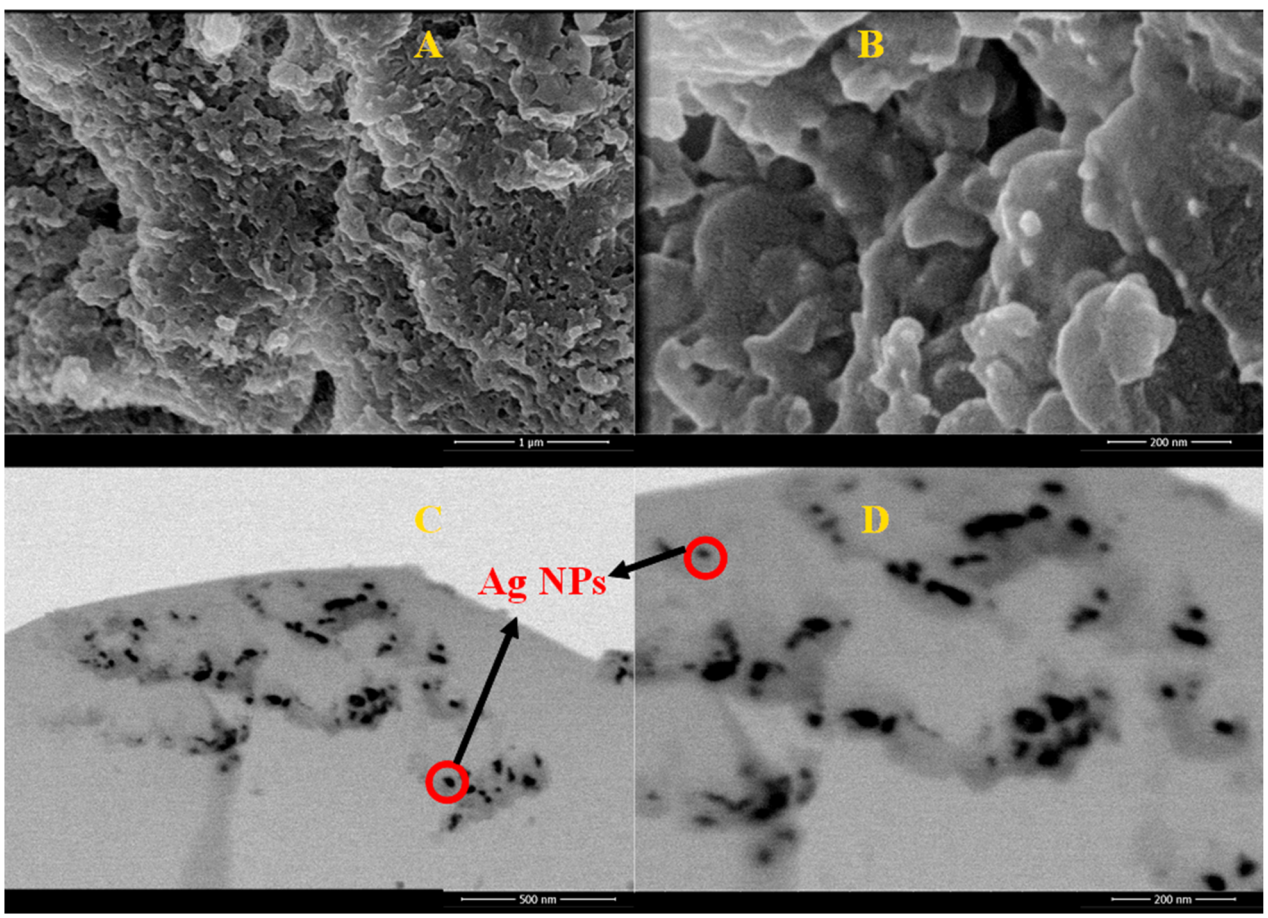

Fig. 4 (A and B) SEM results of AN-P(NM) and (C and D) TEM images of Ag-AN-P(NM).

Below this temperature (VPTT, $T < 305$ K), the shrinkage of AN-P(NM) was minimal, but it became more pronounced as the temperature exceeded 306 K. This deswelling behavior led to an increase in the refractive index of the Ag nanoparticles encapsulated within the AN-P(NM) microgels, resulting in a red shift in the λ_{SPR}. Li *et al.*[85] also reported that the λ_{SPR} of NPs in microgels showed red shifting along with a hyperchromic effect on increasing the temperature (293 K to 323 K).

The effect of pH on the λ_{SPR} value of Ag-AN-P(NM) was also investigated. At a low pH (pH > p*K*a of MAAc), the λ_{SPR} value appeared at shorter wavelengths, whereas a red shift in λ_{SPR} was observed as the pH increased. This red shift is attributed to the stimuli-responsive nature of AN-P(NM). The λ_{SPR} shifted from 397 nm to 422 nm as the pH increased from 2.2 to 9.3. At a low pH, the carboxylic groups in AN-P(NM) remain protonated, causing the microgels to exist in a deswelling state. In this state, microgels provide limited space for the Ag NPs in their network. Under these conditions, the surface electrons of the Ag NPs are confined to a smaller surface area, leading to faster oscillation and requiring higher energy (shorter wavelength) for resonance. At a high pH, the carboxylic groups in the AN-P(NM) microgels are deprotonated ($-COO^-$), resulting in electrostatic repulsion between the negatively charged carboxylate ions. This causes the microgels to swell, creating more space for the oscillation of surface electrons. Consequently, the oscillation speed decreases, requiring lower energy (longer wavelength) for coupling with the oscillating surface electrons of the Ag NPs. Therefore, λ_{SPR} of Ag NPs encapsulated in AN-P(NM) microgels shifts to lower energy (higher wavelength) as the pH increases. Additionally, the shifting can be influenced by the aggregation of Ag nanoparticles within the microgels, as the nanoparticles can move from one sieve to another within the swollen microgel network. Red shifting with a hypochromic effect was reported by Farooqi *et al.*[86] as the pH of Ag-P(NIPAM-MAA) increased. However, further study is necessary to completely understand the essential reasons for this behavior.

3.3. Catalytic activity

The analytic activity of Ag-AN-P(NM) hybrid microgels is studied for the reduction of both nitro and aldehyde groups containing

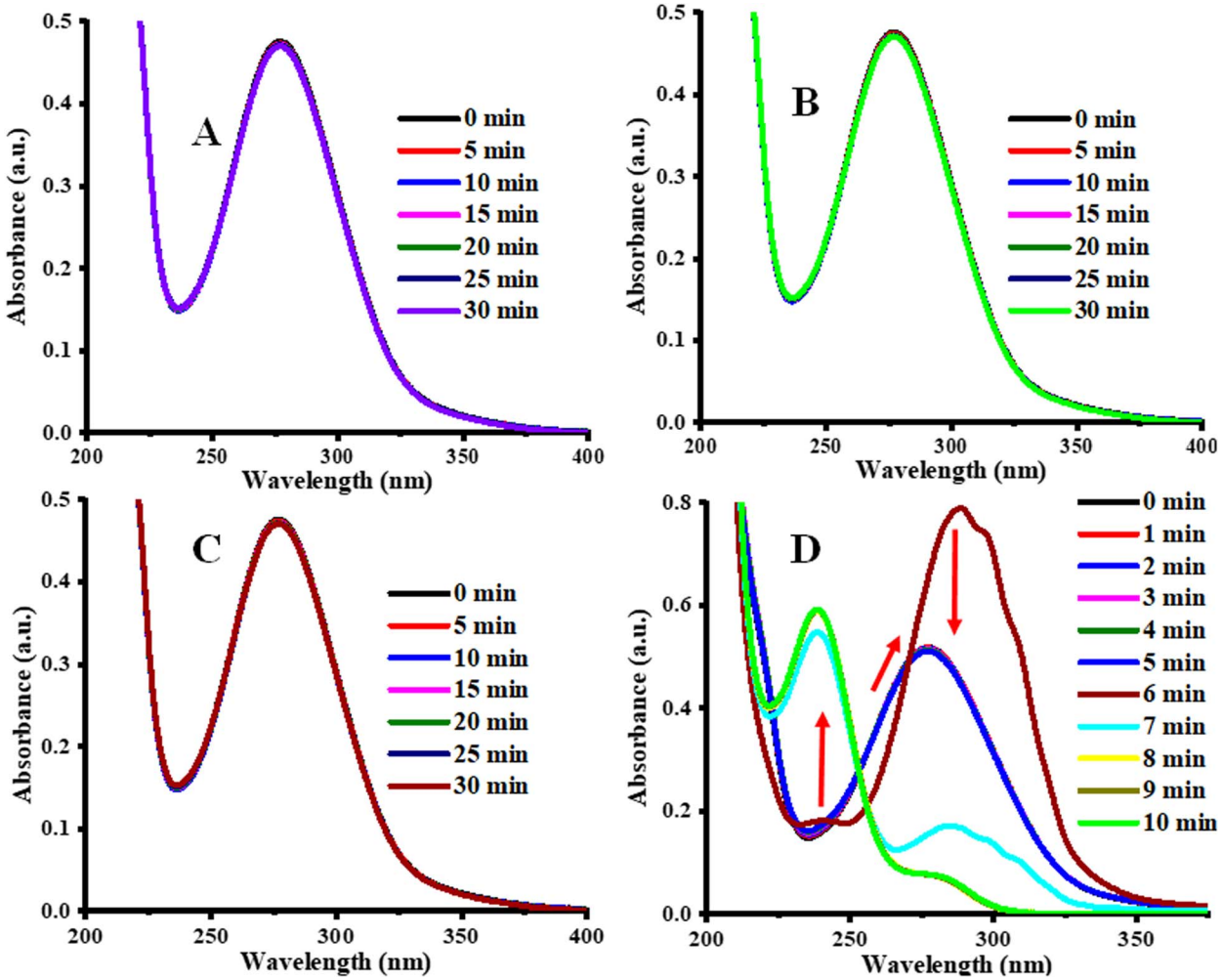

Fig. 5 Controlled experiments for reduction: (A) conditions: [4NBA] = 0.049 mM and Ag-AN-P(NM) = 1.48 mg mL^{-1} in the absence of $NaBH_4$; (B) conditions: [$NaBH_4$] = 2.66 mM and [4NBA] = 0.049 mM in the absence of Ag-AN-P(NM); (C) conditions: [4NBA] = 0.049 mM, AN-P(NM) = 1.48 mg mL^{-1}, and $NaBH_4$ = 2.66 mM; and (D) conditions: [4NBA] = 0.049 mM, Ag-AN-P(NM) = 1.48 mg mL^{-1}, and [$NaBH_4$] = 2.66 mM.

aromatic compounds. For this purpose, a reduction of 4NBA was used as a model for catalytic performance.

To identify the true substance that showed catalytic activity, some controlled experiments were conducted. In the first case, 1.48 mg mL^{-1} of Ag-AN-P(NM) was placed into 3.5 mL of 4NBA (0.09 mM) solution, and the spectrum was run for 30 min, as shown in Fig. 5(A). The decline in the peak was not observed, which showed that the Ag-AN-P(NM) hybrid microgel did not reduce to the 4NBA in the absence of reductant ($NaBH_4$). In the second case, 1.5 mL of $NaBH_4$ (6.21 mM) was placed into 2 mL of 4NBA (0.09 mM), and the spectrum was observed. The results showed that no reduction occurred with $NaBH_4$ alone, as shown in Fig. 5(B). This revealed that $NaBH_4$ alone did not reduce the 4NBA. In the third case, 1.5 mL of $NaBH_4$ (6.21 mM) and 1.48 mg mL^{-1} of AN-P(NM) were added into 2 mL of 4NBA (0.09 mM) and run for 30 min, as illustrated in Fig. 5(C). A reduction was not observed, which indicated that the AN-P(NM) microgel did not act as a catalyst. In the last case, 1.48 mg mL^{-1} of Ag-AN-P(NM) and 1.5 mL of $NaBH_4$ (6.21 mM) were added into 2 mL of 4NBA (0.09 mM) solution, and the spectrum was run for 10 min, as shown in Fig. 5(D). This time, the peak height shifted from 276 nm to a longer wavelength (290 nm) with a higher peak height and then began to decrease continuously. Simultaneously, a new peak appeared at 238 nm, which revealed the shifting of 4NBA into 4ABA, as shown in Fig. 5(D). After 8 min, no further decline in the peak was observed, which indicated that the reduction of 4NBA was completed. This reduction clearly indicated that Ag-AN-P(NM) showed catalytic activity owing to the presence of Ag nanoparticles only, and reduction occurred only along with $NaBH_4$. In the structure of 4NBA, two (nitro and aldehyde) groups were present, which were reduced during this catalytic reduction reaction. The reduction of the aldehyde group is easier than the nitro group. Therefore, aldehyde groups were reduced first, followed by nitro groups. During the reduction of the aldehydic groups, the wavelength of the substrate shifted towards a longer wavelength along with higher intensity, while this peak decreased continuously during the reduction of the nitro groups. Initially, the value of λ_{max} of 4NBA appeared at 276 nm. When the reduction of 4NBA started, λ_{max} increased to 290 nm, which finally decreased, while a new peak appeared at 238 nm owing to 4ABA.

3.3.1. Kinetic study. To study the chemical kinetics of the catalytic reduction of 4NBA, a pseudo-order kinetic equation was used. The reduction was performed in the presence of Ag-AN-P(NM) along with an excess amount of $NaBH_4$ compared to the concentration of 4NBA. The apparent rate constant (k_{ob}) value was determined by applying eqn (1):

$$\ln\frac{A_t}{A_o} = k_{ob}t + C, \quad (1)$$

where A_t, A_o, and t represent the absorbance value at any time (t), the initial absorbance value, and any time of the catalytic reduction reaction, respectively. k_{ob} and C are the apparent rate constant and the intercept, respectively. The value of k_{ob} was obtained from the slope of a graph plotted between $\ln(A_t/A_o)$ and time. The relationship of $\ln(A_t/A_o)$ with time is divided into three portions. In the first portion, the value of $\ln(A_t/A_o)$ did not change with respect to time, which is called the induction period (t_{in}), and it is a characteristic of heterogeneous catalysis. The second portion in which $\ln(A_t/A_o)$ linearly decreased with time is called reaction time (t_{re}). This is the time during which the 4NBA is converted into 4ABA. After t_{re}, the $\ln(A_t/A_o)$ value becomes constant with time, which is called the completion time (t_{co}). This is the time in which all molecules of 4NBA are converted into 4ABA. The t_{re} was used for the calculation of the slope, which is equal to the k_{ob} value.

According to Beer–Lambert law, the absorbance value is directly related to the concentration of the substance. During the catalytic reduction, the concentration of 4NBA was first converted into 4-nitrobenzyl alcohol (4NBlA), which was indicated by shifting the peak from 276 nm to 296 nm. During the reduction of nitro-groups, the peak height of 4NBlA decreased, and a new peak appeared at 238 nm.[87] The catalytic reduction of aldehydic groups was very fast. Therefore, this reduction was not used for the chemical kinetics. More studies are required to be conducted on this conversion of aldehydic groups into alcoholic groups with respect to reaction kinetics. The reduction rates of these reactions were studied using the absorbance of 4NBlA (296 nm). The decline in the absorbance of 4NBlA during reduction was used to calculate the k_{ob} value.

The catalytic reduction of 4NBA was performed under different reaction conditions, such as the concentrations of 4NBA, $NaBH_4$, catalytic dose, and temperature. The reduction of 4NBA was performed by varying the concentration of $NaBH_4$ from 1.97 mM to 6.71 mM while keeping the other parameters constant (4NBA concentration = 0.049 mM, Ag-AN-P(NM) = 1.48 mg mL^{-1}, and temperature = 301 K). The graph between $\ln(A_t/A_o)$ *vs.* reduction time for 4NBA under different concentrations of $NaBH_4$ is shown in Fig. 2S(A).† $\ln(A_t/A_o)$ value decreased gradually as the reduction time increased. The values of k_{ob} were determined from the linear decline portion of this graph, as depicted in Fig. 2S(B).†

The $NaBH_4$ content effect on k_{ob} is illustrated in Fig. 2S(B).† The value of k_{ob} was first increased to some extent as the $NaBH_4$ concentration increased but decreased on further increasing the $NaBH_4$ concentration. The value of k_{ob} increased from 0.399 to 2.738 min^{-1} by increasing the concentration of $NaBH_4$ from 1.973 to 5.127 mM. Further increasing the concentrations of $NaBH_4$ decreased the value of k_{ob}. The distance between the reactant ($NaBH_4$) and the surface of the Ag nanoparticles decreased as the content of the reactant increased. Therefore, $NaBH_4$ rapidly reached the Ag nanoparticle surface as the concentration increased, resulting in a decrease in the value of t_{in}. Therefore, the reduction rate initially increased with an increase in $NaBH_4$. These k_{ob} values increased to 5.127 mM of $NaBH_4$. The H_2 molecules (produced from $NaBH_4$) occupied mostly the surface of Ag NPs. Therefore, the availability of the Ag nanoparticle surface decreased to 4NBA. Therefore, the reduction rate of 4NBA decreased upon further increasing the $NaBH_4$ concentration. This indicated that both H_2 and 4NBH were adsorbed on the Ag nanoparticle surface for catalytic reduction.[88] Complete details of the reduction of 4NBA under different concentrations of 4NBA, catalytic dose and concentration of $NaBH_4$ are illustrated in Table 1.

Table 1 Catalytic reduction conditions of 4NBA along with induction time (t_{in}), apparent rate constant (k_{ob}), completion time (t_{co}) and half-life period ($t_{1/2}$) at different concentrations of 4NBA, $NaBH_4$ Ag-AN-P(NM) dose, and temperature

Reaction condition	$NaBH_4$ (mM)	Ag-AN-P(NM) (mg mL^{-1})	4NBA (mM)	T (°C)	t_{in} (min)	t_{co} (min)	k_{ob} (min^{-1})	$t_{1/2}$ (min)
$NaBH_4$	1.97	1.48	0.049	28	13	19	0.40	1.73
	2.66	1.48	0.049	28	5	9	0.93	0.75
	3.55	1.48	0.049	28	5	8	1.14	0.61
	4.34	1.48	0.049	28	3	6	1.19	0.58
	5.13	1.48	0.049	28	3	5	2.74	0.25
	5.92	1.48	0.049	28	4	8	0.78	0.89
	6.71	1.48	0.049	28	4	9	0.55	1.26
Ag-AN-P(NM)	3.55	0.59	0.057	28	13	22	0.28	2.47
	3.55	0.89	0.057	28	7	12	0.74	0.94
	3.55	1.19	0.057	28	4	8	0.90	0.77
	3.55	1.48	0.057	28	3	6	1.14	0.61
	3.55	1.78	0.057	28	2	4	1.48	0.47
4NBA	3.55	1.48	0.03	28	4	11	0.37	1.87
	3.55	1.48	0.04	28	4	9	0.54	1.28
	3.55	1.48	0.05	28	3	6	1.14	0.61
	3.55	1.48	0.07	28	4	8	0.79	0.88
	3.55	1.48	0.1	28	6	12	0.47	1.47
	3.55	1.48	0.12	28	6	12	0.44	1.57
	3.55	1.48	0.15	28	6	13	0.36	1.92
Temp.	3.55	1.48	0.057	297	3	9	0.98	0.71
	3.55	1.48	0.057	301	2	7	1.15	0.60
	3.55	1.48	0.057	305	1	6	1.27	0.55
	3.55	1.48	0.057	309	2	7	1.14	0.61
	3.55	1.48	0.057	313	2	7	1.10	0.63

The reduction of 4NBA was also performed at different concentrations of 4NBA. For this purpose, the 4NBA concentration was changed from 0.03 mM to 0.15 mM while keeping the concentration of $NaBH_4$ and the catalyst constant at 3.55 mM and 1.5 μM, respectively. The rate of 4NBA reduction was increased by increasing the 4NBA concentration from 0.03 to 0.05 mM. The distance between the Ag nanoparticle surface and 4NBA decreased with an increase in concentration. Therefore, more 4NBA molecules rapidly reached the Ag nanoparticles through the crosslinked network and converted rapidly into the product. Therefore, the value of k_{ob} increased while t_{in} decreased with an increase in concentration. The reduction rate decreased by increasing the content from 0.05 to 0.15 mM. As we know, the number of collisions increases as the concentration increases. Therefore, the number of collisions increased as the content increased from 0.05 to 0.15 mM. Therefore, the diffusion rate of reactants across the crosslinked network decreased, resulting in a decrease in the reduction rate. The relation between $\ln(A_t/A_o)$ and reduction time at various 4NBA concentrations is shown in Fig. 3S(A),† and the relation of k_{ob} with 4NBA concentration is depicted in Fig. 3S(B).† The k_{ob} value for the 4NBA reduction increased by increasing the concentration of 4NBA from 0.03 to 0.05 mM and then decreased by increasing the content from 0.05 to 0.15 mM, as shown in Fig. 3S(B).† This reduction behavior of 4NBA also indicated that both reactants (4NBA and H_2) were adsorbed on Ag nanoparticles during the conversion of the 4NBA into 4ABA.[89]

The effect of the catalytic dose on the reduction rate of 4NBA was also studied. For this purpose, the dose of the Ag-AN-P(NM) hybrid microgel was altered from 0.59 to 1.78 mg mL^{-1} while keeping the other parameters constant (4NBA = 0.049 mM, $NaBH_4$ = 3.55 mM, and temperature = 301 K). The k_{ob} value increased continuously as the Ag-AN-P(NM) content increased. The content of Ag NPs increased as the content of Ag-AN-P(NM) increased. Therefore, the surface of the Ag nanoparticles increased because of increasing their content. Hence, more reactant molecules can come and adsorb on the Ag NP surface and rapidly convert into the product. The k_{ob} values of 4NBA reduction reactions were obtained from the graph that was plotted between $\ln(A_t/A_o)$ and Ag-AN-P(NM) content, as depicted in Fig. 6(A). The relationship between the Ag-AN-P(NM) dose and k_{ob} is shown in Fig. 6(B). This graph showed that the value of k_{ob} increased linearly with the Ag-AN-P(NM) dose. The Ag-AN-P(NM) concentration increases, resulting in an increase in the Ag nanoparticle surface area (owing to an increase in the Ag NP content in the medium). Therefore, the active sites increased with an increase in the Ag-AN-P(NM) dose, and the reduction of 4NBA occurred rapidly. A similar increase in the catalytic efficiency of hybrid microgels with a catalytic dose was reported by Ahmad *et al.*[90] for the reduction of nitroarenes.

3.4. Thermodynamic aspects

To examine the effect of temperature on the reduction rate of 4NBA, the reduction reaction was carried out at different temperatures while keeping other parameters constant. To evaluate the k_{ob} values at different temperatures, a plot of $\ln(A_t/A_o)$ *versus* time at different temperatures is presented in Fig. 7(A). The found values of k_{ob} for the 4NBA reduction at

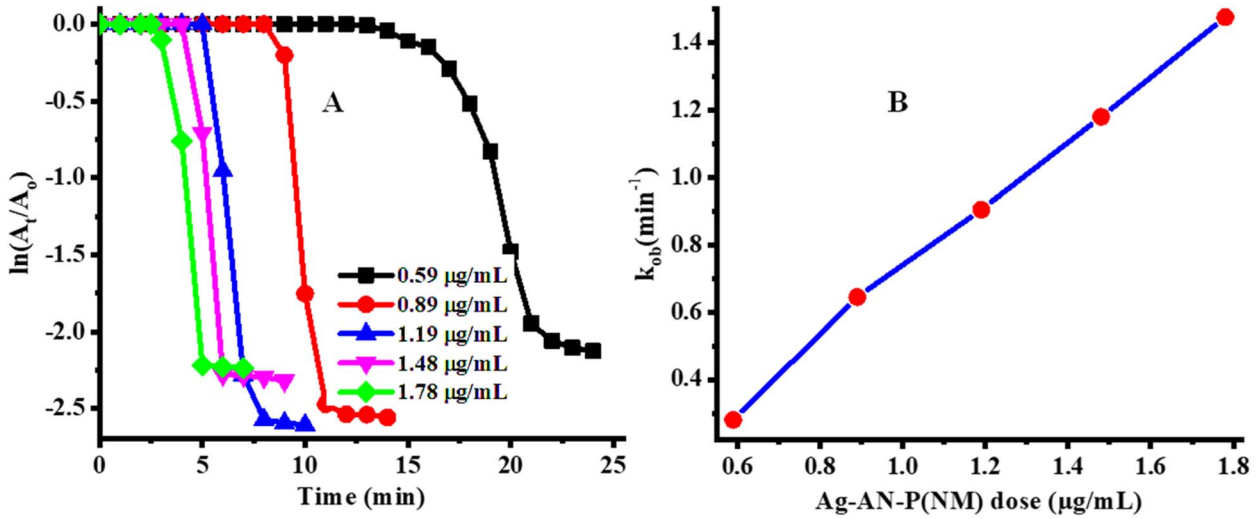

Fig. 6 Catalytic reduction of 4NBA: (A) effect of the amount of the catalyst [conditions: Ag-AN-P(NM) = 0.59–1.78 mg mL^{-1}, [4NBA] = 0.049 mM, and [$NaBH_4$] = 3.55 mM] (B) graph between k_{ob} and catalytic dose.

diverse temperatures are summarized in Table 1. Fig. 7(B) shows the influence of temperature on k_{ob}. A graph of ln k_{ob} *vs.* $1/T$ is plotted to calculate the Arrhenius parameters, as shown in Fig. 7(C). This figure demonstrates that the reduction rate of 4NBA in the Ag-AN-P(NM) dispersion follows the Arrhenius trend at temperatures ranging from 297 to 313 K. Notably, these temperature values lie under the VPTT of AN-P(NM), but deviations were observed after 305 K because of the shrinkage behavior.[91]

The k_{ob} initially increased from 0.976 to 1.273 min^{-1} as the medium temperature increased from 297 to 305 K during the reduction of 4NBA. This increase in k_{ob} with increasing temperature is attributed to a higher proportion of reactants with kinetic energy (E_k) ≥ activation energy (E_a). As the medium temperature increased, the E_k of the reactants surpassed E_a, enabling them to diffuse more rapidly across the polymeric structure of Ag-AN-P(NM). Consequently, higher k_{ob} values were observed, which was consistent with typical Arrhenius behavior in the 297–305 K range. However, a fall in k_{ob} was observed beyond 305 K. This behavior of Ag-AN-P(NM) is attributed to the deswelling nature of AN-P(NM), which decreases the accessibility of reactants to the Ag NP surface. Consequently, k_{ob} reduced further as temperature increased owing to deswelling behavior till 313 K. A similar reduction trend for 4NiA was described by Shahid *et al.*[92] using Ag-P(NIPAM-AAm-MAA).

Using eqn (2), the value of E_a was determined with the slope obtained from the $1/T$ *vs.* ln k_{ob} plot, while the pre-exponential factor (A) was found from the intercept, as shown in Table 2.

$$\ln k_{ob} = -\frac{E_a}{R}\left(\frac{1}{T}\right) + \ln A, \quad (2)$$

where A represents the pre-exponential factor and E_a is the observed activation energy for the reduction reaction using an Ag-AN-P(NM) catalyst. The activation entropy (ΔS^*) and activation enthalpy (ΔH^*) for these reduction reactions were determined using Eyring eqn (3). To calculate these parameters, a plot of $\ln(k_{ob}/T)$ *versus* $1/T$ was generated, as shown in Fig. 7(D).

$$\ln\left(\frac{k_{ob}}{T}\right) = -\frac{\Delta H^*}{R}\left(\frac{1}{T}\right) + \ln\left(\frac{k_B}{h}\right) + \frac{\Delta S^*}{R}, \quad (3)$$

where h and k_B represent the Planck's constant and Boltzmann's constant, respectively, and 6.63×10^{-34} Js and 1.38×10^{-23} JK^{-1} are their values, respectively. The R indicates the general gas constant. The E_a, ΔH^*, A, and ΔS^* values for 4NBA reduction with Ag-AN-P(NM) at various temperatures are presented in Table 2.

The activation enthalpy (ΔH^*) was found to be positive (22.529 kJ mol^{-1}), indicating that the formation of the activated complex during the catalytic reduction of 4NiA is an endothermic process. The activation entropy (ΔS^*) value of −0.582 kJ mol^{-1} K^{-1} indicates that the reduction of 4NBA using Ag-AN-(NM) is more suitable at higher temperatures.

3.5. Proposed reduction mechanism

The catalytic reduction behavior of 4NBA under various concentrations of $NaBH_4$ and 4NBA with Ag-AN-P(NM) indicated that the catalytic reduction of 4NBA followed the Langmuir Hinshelwood mechanism, as shown in Fig. 8. According to this mechanism, BH_4^- ions (produced from $NaBH_4$) were diffused along with 4NBA molecules into the network of Ag-AN-P(NM). The diffused BH_4^- ions produced H_2 that is attached to the Ag nanoparticle surface. Similarly, 4NBA molecules were also diffused and adsorbed on the Ag nanoparticle surface. H_2 molecules interacted with the 4NBA molecules on the surface of the Ag NPs, which acted as an electron conveyor belt, first reducing the 4NBA into 4-nitrobenzylalcohol (4NBlA) and then reducing 4ABlA into 4ABlA. In this reaction, 4NBA acted as an electrophilic species, while BH_4^- ions acted as nucleophilic species. The BH_4^- ions transfer their electrons to 4NBA through the Ag nanoparticle surface along with hydrogen.[36] Hydride

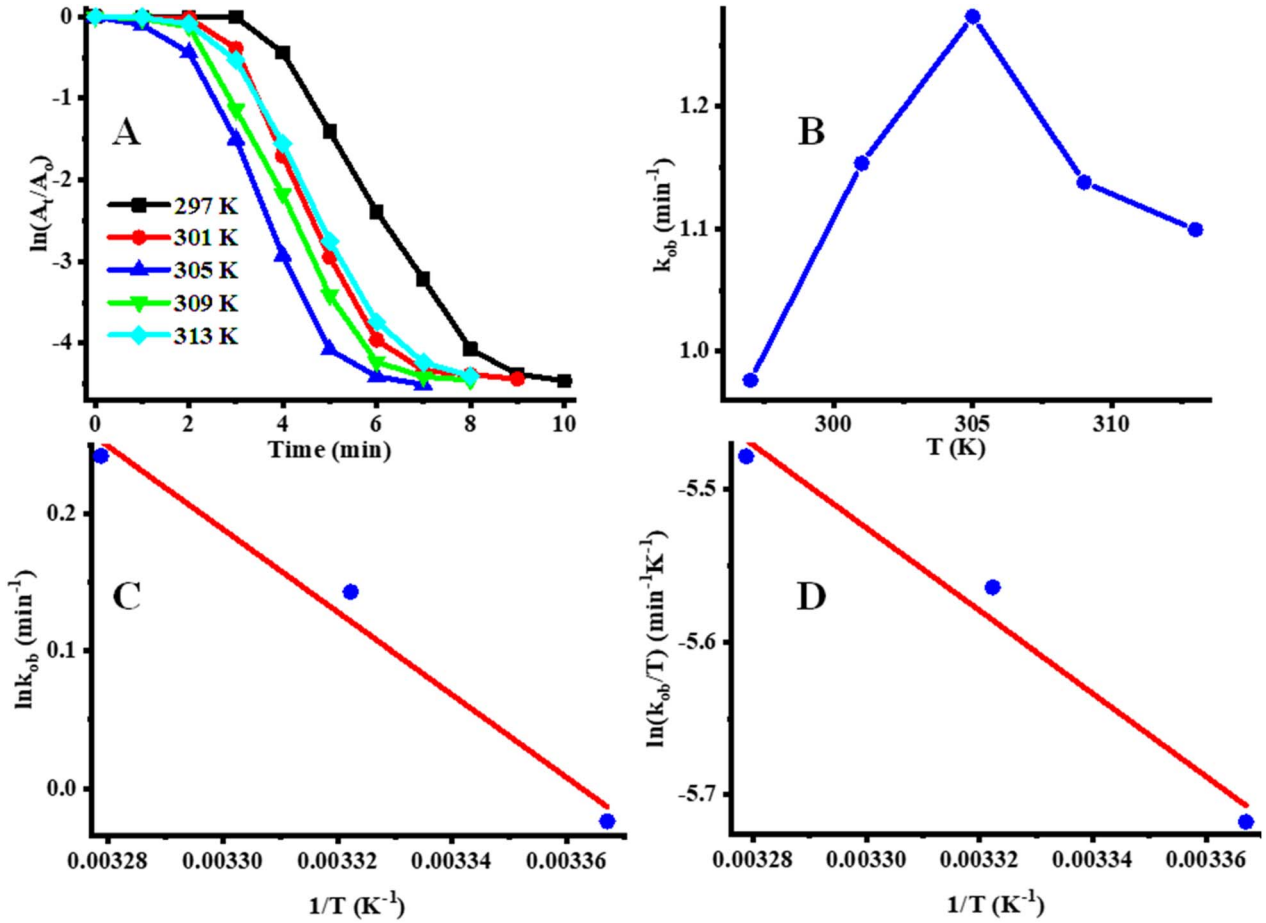

Fig. 7 Catalytic reduction of 4NBA under different temperatures (297–313 K) illustrated as follows: (A) time *vs.* $\ln(A_t/A_o)$ under different temperatures [conditions: 4NBA concentration = 0.049 mM, [$NaBH_4$] = 3.55 mM, and Ag-AN-P(NM) = 1.48 mg mL^{-1}], (B) k_{ob} *vs.* temperature, (C) Arrhenius, and (D) Eyring plot.

Table 2 E_a, ΔH^*, ΔS^*, and A for 4NBA reduction with Ag-AN-P(NM)

Kinetics/thermodynamic parameters	Value
E_a (kJ mol^{-1})	25.031
A (min^{-1})	2.492×10^4
ΔH^* (kJ mol^{-1})	22.529
ΔS^* (kJ mol^{-1} K^{-1})	−0.582

from BH_4^- attacks the carbon of the aldehydic group, and oxygen of this aldehydic group attacks the proton of water, resulting in the formation of product a, as shown in Fig. 8. In the next step, a hydride from BH_4^- is attached with oxygen and proton with other oxygen atoms of the nitro group to form product b. Then, proton shifting occurs, and a water molecule eliminates the formation of products c and d, respectively. The oxygen of the d intermediate attaches to a proton and hydride with nitrogen to form e and then product f with a similar attachment of atoms. This product (f) detached from the Ag NP surface and moved across the network to the bulk medium.[43]

3.6. Reduction of others

The reduction of 3NBA and 3,5DNBA was also performed under similar conditions. The UV-vis spectra are depicted in Fig. 4S(A and B).† The values of k_{ob} for their reduction were achieved by applying a pseudo first order kinetic equation. The catalytic reduction rate indicated that the reduction order of these compounds is as follows: 3NBA > 4NBA > 3,5DNBA. The catalytic reduction rate of 3NBA was found to be greater than that of 4NBA and 3,5DNBA. Basically, the electrons are shifted from BH_4^- to reductant (NBA derivatives) through the surface of the metal nanoparticles. This electron transporting has occurred rapidly on these compounds, which have more electron deficiencies. In 4NBA, which was first converted into 4NBlA, the structure of 4NBlA has electron donating (–CH_2OH) and electron withdrawing (–NO_2) groups opposite to each other. In addition, these are present in 1st and 4th positions. Therefore, electronic clouds are easily transferred from –CH_2OH to –NO_2 compared to the 1st and 3rd positions, as shown in 3NBA (the 1st and 3rd positions of the benzene ring are not involved in the resonance). Therefore, 3NBA reduced more rapidly than 4NBA, while 4NBA reduced more rapidly than 3,5DNBA owing to fewer reduction (–NO_2) groups in its structure. In the case of 3,5DNBA,

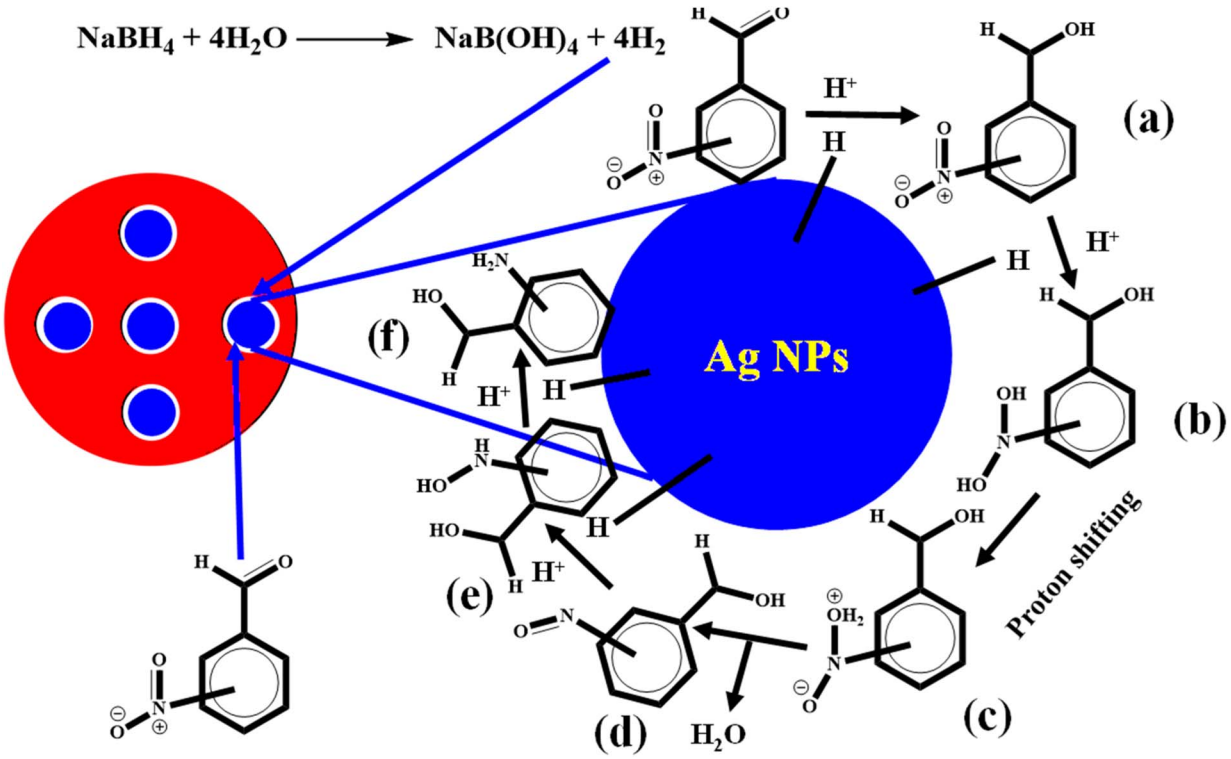

Fig. 8 Reduction mechanism of 4NBA derivatives.

the two $-NO_2$ groups were reduced simultaneously, while only one $-NO_2$ group for 4NBA and the reduction of two $-NO_2$ groups took more time than one $-NO_2$ group. This is why 4NBA reduced more rapidly than 3,5DNBA.[93]

3.7. Catalytic activity comparison

The catalytic performance of Ag-AN-P(NM) was compared with the others, as summarized in Table 3. The results indicate that Ag-AN-P(NM) stands out as the best catalyst owing to its high catalytic activity, stimuli-responsive performance, reusability, and exceptional stability. Although other catalysts may exhibit one, two, or at most three of these properties, the Ag-AN-P(NM) hybrid microgel system integrates all these advantages. Consequently, it emerges as the most effective choice for catalytic reduction reactions.

3.8. Recycling

The recycling ability of Ag-AN-P(NM) was evaluated using the reduction of 4NBA as a model. After completing each reaction cycle, the Ag-AN-P(NM) was recovered through centrifugation. The recovered catalytic content was then reused for the reduction of 4NBA under identical conditions. The k_{ob} value for each cycle was determined, and the percentage catalytic efficiency of Ag-AN-P(NM) was calculated using the following equation:

$$\text{Percentage catalytic efficiency}(\%) = \frac{k_{ob}(n\text{th cycle})}{k_{ob}(1\text{st cycle})} \times 100. \quad (4)$$

The percentage of catalytic performance of the Ag-AN-P(NM) system across multiple recycling cycles is shown in Fig. 9. No significant decline in activity was noted with an increasing number of cycles, with the system retaining 91% of its catalytic efficiency even after four cycles. The slight reduction in activity is likely due to minor losses of catalysts during the centrifugation and decantation steps involved in the recycling process. Post-reuse characterization of Ag-AN-P(NM) using FTIR and XRD techniques, as depicted in Fig. 5S(A) and (B),† respectively, revealed identical peaks, confirming that the recycled material remained Ag-AN-P(NM).

Table 3 Catalytic performance comparison with other systems

Catalysts	NPs stability	Effect of temperature (T)	Maximum k_{ob} (min^{-1})	References
Ni-RGO	No	—	0.013	94
Ag-P(NIPAM-AA)	Yes	—	0.415	95
P(NIPAM)@Ag-P(HEMA)	Yes	T = 21–30	0.127–0.232	89
Ag NPs	No	—	0.011	96
Ag-P(NIPMAM-MAA)	Yes	—	0.9907	51
Ag-AN-P(NM)	Yes	T = 24–32	0.57–0.95, max = 1.34	Present work

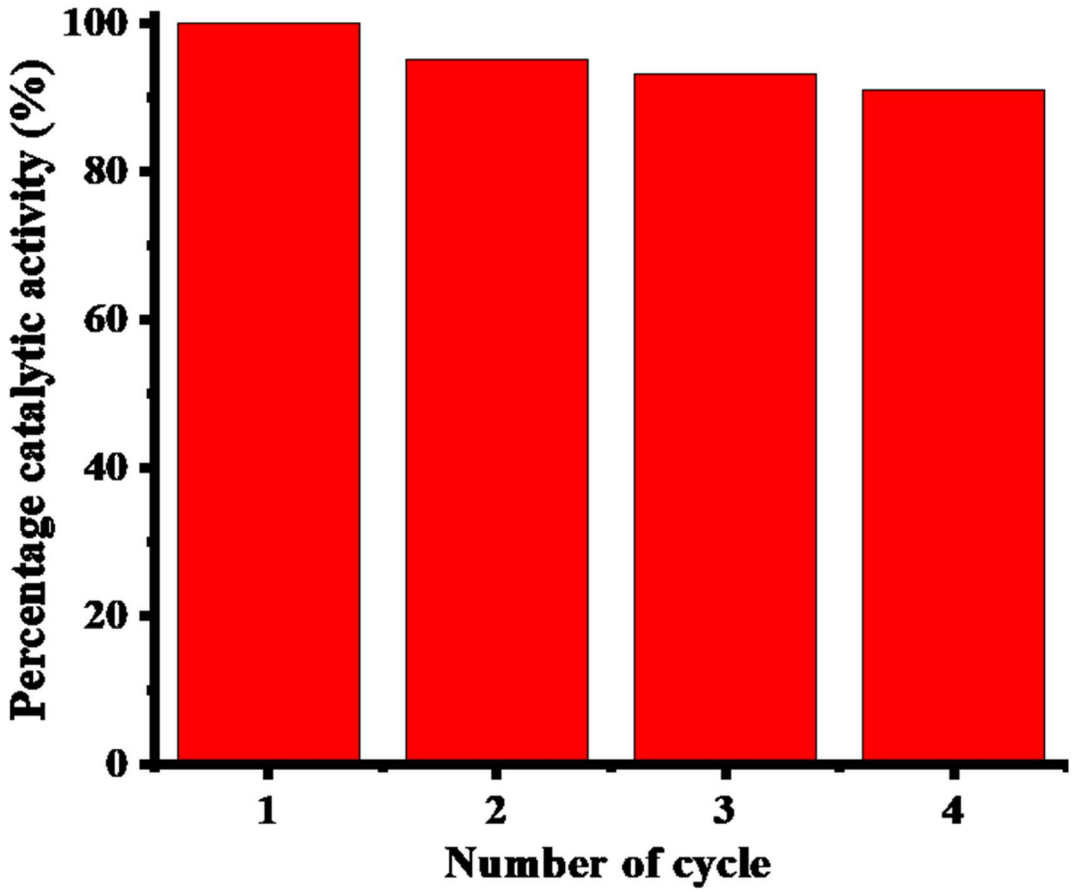

Fig. 9 Catalytic activity during recycling [conditions: [4NBA] = 0.049 mM, Ag-AN-P(NM) = 1.48 mg mL^{-1}, and [BH_4^-] = 3.55 mM].

4. Conclusion

AN-P(NM) system was synthesized using a free radical precipitation polymerization method in water. Ag NPs were then successfully incorporated into AN-P(NM). The Ag-AN-P(NM) showed both temperature and pH-responsive behavior owing to NIPAM and MAA, respectively. The Ag-AN-P(NM) showed outstanding catalytic efficiency for the reduction of nitrobenzaldehyde derivatives and rapidly converted them into their corresponding amino-benzyl alcohol under mild conditions in an aqueous environment. Both (–NO_2 and –CHO) groups of nitro-benzaldehyde derivatives are reduced stepwise. The –CHO group was first reduced, followed by the –NO_2 groups. Furthermore, the Ag-AN-P(NM) catalytic system demonstrated excellent recyclability, and only a slight reduction in efficiency over repeated use was achieved.

Data availability

Data will be provided on request.

Conflicts of interest

There is no conflict of interest.

Acknowledgements

Authors extend their appreciation to the Deanship of Scientific Research, King Saud University, for funding through Vice Deanship of Scientific Research Chairs, Research Chair for Biomedical Application of Nanomaterials.

References

1 P. K. Singh, U. Kumar, I. Kumar, A. Dwivedi, P. Singh, S. Mishra, C. S. Seth and R. K. Sharma, *Environ. Sci. Pollut. Res.*, 2024, **31**, 56428–56462.
2 H. Kolya and C. W. Kang, *Toxics*, 2024, **12**, 111.
3 P. Babuji, S. Thirumalaisamy, K. Duraisamy and G. Periyasamy, *Water*, 2023, **15**, 2532.
4 R. Noor, A. Maqsood, A. Baig, C. B. Pande, S. M. Zahra, A. Saad, M. Anwar and S. K. Singh, *Urban Clim.*, 2023, **48**, 101413.
5 P. Kovacic and R. Somanathan, *J. Appl. Toxicol.*, 2014, **34**, 810–824.
6 M. Bilal, A. R. Bagheri, P. Bhatt and S. Chen, *J. Environ. Manage.*, 2021, **291**, 112685.
7 K. H. Vardhan, P. S. Kumar and R. C. Panda, *J. Mol. Liq.*, 2019, **290**, 111197.
8 Z. Wang, P. Luo, X. Zha, C. Xu, S. Kang, M. Zhou, D. Nover and Y. Wang, *J. Clean. Prod.*, 2022, **379**, 134043.

9 M. Ismail, K. Akhtar, M. I. Khan, T. Kamal, M. A. Khan, A. M. Asiri, J. Seo and S. B. Khan, *Curr. Pharm. Des.*, 2019, **25**, 3645–3663.
10 T. Islam, M. R. Repon, T. Islam, Z. Sarwar and M. M. Rahman, *Environ. Sci. Pollut. Res.*, 2022, **30**, 9207–9242.
11 E. Wołejko, A. Jabłońska-Trypuć, U. Wydro, A. Butarewicz and B. Łozowicka, *Appl. Soil Ecol.*, 2020, **147**, 103356.
12 A. Trajanov, V. Kuzmanovski, B. Real, J. M. Perreau, S. Džeroski and M. Debeljak, *Environ. Sci. Pollut. Res.*, 2018, **25**, 18781–18792.
13 X. Chen, Q. Luo, D. Wang, J. Gao, Z. Wei, Z. Wang, H. Zhou and A. Mazumder, *Environ. Pollut.*, 2015, **206**, 64–72.
14 A. Ahmed Laskar and H. Younus, *Drug Metab. Rev.*, 2019, **51**, 42–64.
15 S. Manzetti, *Environ. Chem. Lett.*, 2012, **10**, 349–361.
16 G. Sabbioni, *Chem. Res. Toxicol.*, 2017, **30**, 1733–1766.
17 G. Sabbioni and C. R. Jones, *Biomarkers*, 2002, **7**, 347–421.
18 J. Qiu, B. Tang, B. Ju, Y. Xu and S. Zhang, *Dyes Pigm.*, 2017, **136**, 63–69.
19 X. Yu, H. Liu, J. Diao, Y. Sun and Y. Wang, *Sep. Purif. Technol.*, 2018, **204**, 213–219.
20 H. Xu, J. L. Shi, H. Hao, X. Li and X. Lang, *Catal. Today*, 2019, **335**, 128–135.
21 M. Naim, M. F. Mohammat, P. N. A. Mohd Ariff and M. H. Uzir, *Enzyme Microb. Technol.*, 2024, **180**, 110483.
22 D. Ghislieri, A. P. Green, M. Pontini, S. C. Willies, I. Rowles, A. Frank, G. Grogan and N. J. Turner, *J. Am. Chem. Soc.*, 2013, **135**, 10863–10869.
23 V. Froidevaux, C. Negrell, S. Caillol, J.-P. Pascault and B. Boutevin, *Chem. Rev.*, 2016, **116**, 14181–14224.
24 M. Aslam, M. A. Kalyar and Z. A. Raza, *Polym. Eng. Sci.*, 2018, **58**, 2119–2132.
25 J. Jin and D. W. C. MacMillan, *Nature*, 2015, **525**(7567), 87–90.
26 C. Gunanathan, Y. Ben-David and D. Milstein, *Science*, 2007, **317**, 790–792.
27 C. Li, J. Wang, M. Ning and H. Zhang, *J. Appl. Polym. Sci.*, 2012, **124**, 4127–4135.
28 A. Torres de Pinedo, P. Peñalver and J. C. Morales, *Food Chem.*, 2007, **103**, 55–61.
29 G. Guillena, D. J. Ramón and M. Yus, *Chem. Rev.*, 2010, **110**, 1611–1641.
30 D. Pingen and D. Vogt, *Catal. Sci. Technol.*, 2013, **4**, 47–52.
31 L. U. Nordstrøm, H. Vogt and R. Madsen, *J. Am. Chem. Soc.*, 2008, **130**, 17672–17673.
32 S. Hazra, E. Malik, A. Nair, V. Tiwari, P. Dolui and A. J. Elias, *Chem.–Asian J.*, 2020, **15**, 1916–1936.
33 M. Arif, H. Raza and T. Akhter, *J. Mol. Liq.*, 2025, **419**, 126762.
34 M. Arif, H. Raza, F. Tahir, S. Ben Moussa, S. M. Haroon, A. Y. Abdullah Alzahrani and T. Akhter, *J. Mol. Liq.*, 2024, **416**, 126516.
35 M. Arif, A. Rauf, H. Raza, S. Ben Moussa, S. M. Haroon, A. Y. A. Alzahrani and T. Akhter, *Int. J. Biol. Macromol.*, 2024, **275**, 133633.
36 R. Begum, Z. H. Farooqi, A. H. Aboo, E. Ahmed, A. Sharif and J. Xiao, *J. Hazard. Mater.*, 2019, **377**, 399–408.
37 A. Call, C. Casadevall, F. Acuña-Parés, A. Casitas and J. Lloret-Fillol, *Chem. Sci.*, 2017, **8**, 4739–4749.
38 M. D. Argyle and C. H. Bartholomew, *Catalysts*, 2015, **5**, 145–269.
39 N. Shambhawi, O. Mohan, T. S. Choksi and A. A. Lapkin, *Catal. Sci. Technol.*, 2024, **14**, 515–532.
40 M. Arif, H. Raza, S. Ben Moussa, A. Y. A. Alzahrani and T. Akhter, *Int. J. Biol. Macromol.*, 2024, **282**, 136906.
41 X. Chen, L. Cheng, J. Gu, H. Yuan and Y. Chen, *Chem. Eng. J.*, 2024, **479**, 147853.
42 S. Batool, M. Langer, S. N. Myakala, M. Heiland, D. Eder, C. Streb and A. Cherevan, *Adv. Mater.*, 2024, **36**, 2305730.
43 M. Arif, M. Shahid, A. Irfan, J. Nisar, W. Wu, Z. H. Farooqi and R. Begum, *RSC Adv.*, 2022, **12**, 5105–5117.
44 H. Zhao, Q. Wang, H. Li, H. Li, T. Han, A. Wang and K. Yao, *J. Alloys Compd.*, 2024, **1006**, 176313.
45 M. Arif, *J. Mol. Liq.*, 2024, **403**, 124869.
46 M. Arif, *Polymers*, 2023, **15**, 3600.
47 M. Arif, Z. H. Farooqi, A. Irfan and R. Begum, *J. Mol. Liq.*, 2021, **336**, 116270.
48 S. Iqbal, N. Iqbal, S. Musaddiq, Z. H. Farooqi, M. A. Habila, S. M. Wabaidur and A. Iqbal, *Heliyon*, 2024, **10**, e25385.
49 K. Naseem, R. Begum and Z. H. Farooqi, *Polym. Compos.*, 2018, **39**, 2167–2180.
50 A. Haleem, S. B. Syaal, M. Ajmal, J. Ambreen, S. Rauf, N. Ali, S. Muhammad, A. Shah, M. A. Zia and M. Siddiq, *Korean J. Chem. Eng.*, 2020, **37**, 614–622.
51 Z. H. Farooqi, R. Khalid, R. Begum, U. Farooq, Q. Wu, W. Wu, M. Ajmal, A. Irfan and K. Naseem, *Environ. Technol.*, 2019, **40**, 2027–2036.
52 M. Arif, H. Raza, S. M. Haroon, S. Ben Moussa, F. Tahir and A. Y. A. Alzahrani, *Int. J. Biol. Macromol.*, 2024, **270**, 132331.
53 M. Arif, A. Rauf and T. Akhter, *RSC Adv.*, 2024, **14**, 19381–19399.
54 M. Arif, *Mater. Today Commun.*, 2023, **36**, 106580.
55 M. Arif, *J. Mol. Liq.*, 2023, **375**, 121346.
56 M. Arif, *J. Environ. Chem. Eng.*, 2023, **11**, 109270.
57 M. Arif, *RSC Adv.*, 2022, **12**, 15447–15460.
58 G. Liao, Y. Gong, L. Zhong, J. Fang, L. Zhang, Z. Xu, H. Gao and B. Fang, *Nano Res.*, 2019, **12**, 2407–2436.
59 G. Liao, J. Fang, Q. Li, S. Li, Z. Xu and B. Fang, *Nanoscale*, 2019, **11**, 7062–7096.
60 H. Zhu, C. Zhang, K. Xie, X. Li and G. Liao, *Chem. Eng. J.*, 2023, **453**, 139775.
61 S. Liu, Y. Guo, S. Yi, S. Yan, C. Ouyang, F. Deng, C. Li, G. Liao and Q. Li, *Sep. Purif. Technol.*, 2023, **307**, 122727.
62 S. Liu, F. Deng, Y. Guo, C. Ouyang, S. Yi, C. Li, G. Liao and Q. Li, *ACS Appl. Nano Mater.*, 2024, **7**, 889–903.
63 C. Li, H. Lu, G. Ding, Q. Li and G. Liao, *Catal. Sci. Technol.*, 2023, **13**, 2877–2898.
64 Y. Qiao, C. Sun, J. Jian, T. Zhou, X. Xue, J. Shi, G. Che and G. Liao, *J. Mol. Liq.*, 2023, **385**, 122383.
65 M. Arif, *RSC Adv.*, 2023, **13**, 3008–3019.
66 M. Arif, H. Raza and T. Akhter, *RSC Adv.*, 2024, **14**, 24604–24630.

67 R. Begum, Z. H. Farooqi, E. Ahmed, K. Naseem, S. Ashraf, A. Sharif and R. Rehan, *Appl. Organomet. Chem.*, 2017, **31**, 1–8.
68 E. Hermosillo-Ochoa, N. A. Cortez-Lemus and E. A. Reynoso-Soto, *New J. Chem.*, 2024, **48**, 3258–3267.
69 J. Dupont, G. S. Fonseca, A. P. Umpierre, P. F. P. Fichtner and S. R. Teixeira, *J. Am. Chem. Soc.*, 2002, **124**, 4228–4229.
70 L. M. Bronstein and Z. B. Shifrina, *Chem. Rev.*, 2011, **111**, 5301–5344.
71 T. Song, F. Gao, S. Guo, Y. Zhang, S. Li, H. You and Y. Du, *Nanoscale*, 2021, **13**, 3895–3910.
72 M. Arif, *Eur. Polym. J.*, 2024, **206**, 112803.
73 M. Arif, *RSC Adv.*, 2024, **14**, 9445–9471.
74 S. Iqbal, C. Zahoor, S. Musaddiq, M. Hussain, R. Begum, A. Irfan, M. Azam and Z. H. Farooqi, *Ecotoxicol. Environ. Saf.*, 2020, **202**, 110924.
75 K. Naseem, R. Begum, Z. H. Farooqi, W. Wu and A. Irfan, *Appl. Organomet. Chem.*, 2020, **34**, e5742.
76 G. A. Martau, M. Mihai and D. C. Vodnar, *Polymers*, 2019, **11**, 1837.
77 S. Shi, Q. Wang, T. Wang, S. Ren, Y. Gao and N. Wang, *J. Phys. Chem. B*, 2014, **118**, 7177–7186.
78 P. Bhol and P. S. Mohanty, *J. Phys.: Condens. Matter*, 2020, **33**, 084002.
79 H. Naeem, M. Ajmal, S. Z. Khan, M. N. Ashiq and M. Siddiq, *Soft Mater.*, 2021, **19**, 480–494.
80 M. Siddiq, K. Bakhat and M. Ajmal, *Pure Appl. Chem.*, 2020, **92**, 445–459.
81 S. Rahman, F. F. Al-Harbi, M. Ajmal, A. Naseem, Z. H. Farooqi and M. Siddiq, *J. Mater. Sci.*, 2022, **57**, 6763–6779.
82 Z. H. Farooqi, K. Naseem, R. Begum and A. Ijaz, *J. Inorg. Organomet. Polym. Mater.*, 2015, **25**, 1554–1568.
83 M. Arif, F. Tahir, U. Fatima, R. Begum, Z. H. Farooqi, M. Shahid, T. Ahmad, M. Faizan, K. Naseem and Z. Ali, *Mater. Today Commun.*, 2022, 104700.
84 M. Arif, H. Raza and T. Akhter, *RSC Adv.*, 2024, **14**, 38120–38134.
85 L. Li, R. Niu and Y. Zhang, *RSC Adv.*, 2018, **8**, 12428–12438.
86 Z. H. Farooqi, K. Naseem, R. Begum and A. Ijaz, *J. Inorg. Organomet. Polym. Mater.*, 2015, **25**, 1554–1568.
87 M. R. Naimi-Jamal, J. Mokhtari, M. G. Dekamin and G. Kaupp, *Eur. J. Org. Chem.*, 2009, **2009**, 3567–3572.
88 A. Ahmad, P. G. Roy, A. Hassan, S. Zhou, M. Azam, M. A. Z. G. Sial, A. Irfan, F. Kanwal, R. Begum and Z. H. Farooqi, *Int. J. Biol. Macromol.*, 2024, **283**, 137965.
89 G. Mustafa, P. Ghosh Roy, S. Zhou, A. Irfan, A. R. Chaudhry, R. Begum and Z. H. Farooqi, *J. Mol. Liq.*, 2023, **385**, 122397.
90 A. Ahmad, P. G. Roy, S. Zhou, A. Irfan, F. Kanwal, R. Begum and Z. H. Farooqi, *Int. J. Biol. Macromol.*, 2023, **240**, 124401.
91 Z. H. Farooqi, S. R. Khan and R. Begum, *J. Mater. Sci. Technol.*, 2016, **33**, 129–137.
92 M. Shahid, Z. H. Farooqi, R. Begum, K. Naseem, M. Ajmal and A. Irfan, *Korean J. Chem. Eng.*, 2018, **35**, 1099–1107.
93 V. Melinte, L. Stroea, T. Buruiana and A. L. Chibac, *Eur. Polym. J.*, 2019, **121**, 109289.
94 P. Das, S. Ghosh and M. Baskey, *J. Mater. Sci.: Mater. Electron.*, 2019, **30**, 19731–19737.
95 Z. H. Farooqi, A. Ijaz, R. Begum, K. Naseem, M. Usman, M. Ajmal and U. Saeed, *Polym. Compos.*, 2018, **39**, 645–653.
96 T. N. J. I. Edison, E. R. Baral, Y. R. Lee and S. H. Kim, *J. Cluster Sci.*, 2016, **27**, 285–298.